Mode conversion and laser energy absorption by plasma under an inhomogeneous external magnetic field

Srimanta Maity [1,*] Laxman Prasad Goswami [1] Ayushi Vashistha [2,3] Devshree Mandal [2,3] and Amita Das [1,†]

[1]*Department of Physics, Indian Institute of Technology Delhi, Hauz Khas, New Delhi 110016, India*

[2]*Institute for Plasma Research, HBNI, Bhat, Gandhinagar 382428, India*

[3]*Homi Bhabha National Institute, Mumbai 400094, India*

(Received 13 January 2022; accepted 25 April 2022; published 20 May 2022)

The interaction of a high-frequency laser with plasma in the presence of an inhomogeneous external magnetic field has been studied here with the help of particle-in-cell simulations. It has been shown that the laser enters the plasma as an extraordinary wave (X-wave), where the electric field of the wave oscillates perpendicular to both the external magnetic field and propagation direction and as it travels through the plasma, its dispersion property changes due to the inhomogeneity of the externally applied magnetic field. Our study shows that the X-wave's electromagnetic energy is converted to an electrostatic mode as it encounters the upper-hybrid (UH) resonance layer. In the later stage of the evolution, this electrostatic wave breaks and converts its energy to electron kinetic energy. Our study reveals two additional processes involved in decay of the electrostatic mode at the UH resonance layer. We have shown that the energy of the electrostatic mode at the upper-hybrid resonance layer also converts to a low-frequency lower-hybrid mode and high-frequency electromagnetic harmonic radiations. The dependence of energy conversion processes on the gradient of the external magnetic field has also been studied and analyzed.

DOI: 10.1103/PhysRevE.105.055209

I. INTRODUCTION

The absorption of electromagnetic (EM) energy by plasma particles has remained as one of the most important research areas in the context of laser-plasma interaction [1]. Such research is not only of fundamental interests but also has many applications concerning inertial confinement fusion [2–4], particle acceleration schemes [5–11], generation of x-ray [12,13] and γ-ray sources [14], laboratory astrophysics [15], electromagnetic localized structures [16–22], and magnetic field generation [23–26]. In most of these applications, the conversion of EM energy of the incident laser to kinetic energy of plasma particles is essential. There exists many well-known mechanisms, e.g., electron-plasma resonance absorption [27–29], vacuum heating [30], sheath-transit absorption [31,32], and the $\vec{J} \times \vec{B}$ mechanism [33], to heat plasma particles by an intense laser pulse. The first three processes will not work in the case of normal incidence, as in that case, there is no laser electric field component along the direction of the density gradient. The $\vec{J} \times \vec{B}$ mechanism is valid even in the case of normal incidence, but the intensity of the laser should be very high such that the Lorentz force due to the laser magnetic field can no longer be neglected. These energy absorption processes are well explored and require no external magnetic field. However, the presence of an external magnetic field introduces a rich variety of dynamics in the interaction process [34–37]. While the laser cannot penetrate an unmagnetized overdense plasma, it can propagate inside the bulk region of the magnetized plasma. Thus, the presence of an external magnetic field may lead to new unexplored mechanisms related to particle heating in the context of laser-plasma interaction.

One of the most efficient mechanisms for electron heating in a magnetized plasma is the electron-cyclotron-resonance (ECR) [38]. The ECR heating can occur at different EM wave propagation angles and polarizations in the presence of an external magnetic field. In this mechanism, the energy is transferred to plasma particles by cyclotron absorption of the excited waves near harmonics of the ECR. This technique is widely used for heating purpose in fusion plasmas [39–41], plasma thruster [42], along with others. The upper-hybrid (UH) wave, which propagates perpendicular to the external magnetic field, can also be used as an effective tool for plasma heating [43]. In this case, the resonance frequency is the upper hybrid frequency (ω_{uh}), where Lorentz force is responsible for the coupling between electromagnetic and electrostatic components of the field. The wave energy is then transferred irreversibly to plasma particles via collisions or wave-particle interactions near UH resonance. There have been theoretical [44–46], as well as experimental [47–50], works reported where incident microwave energy was absorbed by plasma particles at the UH resonance layer. Lin *et al.* [44] reported the parametric decay of an X-wave at the UH resonance layer to upper-hybrid oscillations and a lower-hybrid mode. Computer simulation results of plasma heating from upper-hybrid mode conversion process were also reported by Lin *et al.* [45]. Their study predicted that the energy of an obliquely incident microwave could be absorbed via wave breaking and

*srimantamaity96@gmail.com

†amita@iitd.ac.in

the electron cyclotron heating induced by parametric instability. Particle-in-cell simulations of the mode conversion and parametric decay instabilities at the upper hybrid layer in magnetically confined fusion plasmas have also been reported in later studies [51,52]. Parametric decay instability near the upper hybrid resonance in magnetically confined fusion plasmas was studied theoretically by Hansen *et al.* [53]. Bryers *et al.* [54] reported the study of parametric instabilities in the context of ionospheric plasma experiments. The excitation of upper-hybrid waves by a thermal parametric instability characterized by a four-wave interaction was reported by Lee *et al.* [55]. Theoretical study of the nonlinear effects concerning the three-wave decay interaction of an extraordinary wave propagating along the density gradient of the plasma was reported by Sharma *et al.* [56].

So far, UH resonance heating in the context of laser-plasma interaction has not been explored in detail. It is mainly because a very high magnetic field is required to magnetize the electrons on the timescale of the incident laser frequency. This high requirement will be fulfilled in the near future as recent work by Nakamura *et al.* [57] reported to have a record of 1200-T laboratory magnetic fields. Thus, it is just a matter of time before the experimental study of UH resonance heating in the context of laser-plasma interaction will be feasible. However, there are some earlier works on the UH wave reported in the context of laser-plasma interaction. Upper-hybrid resonance absorption of laser radiation in a magnetized inhomogeneous plasma was studied theoretically by Grebogi *et al.* [58]. Kitagawa *et al.* [59] reported an experimental study on the upper-hybrid resonance absorption of CO_2-laser under a self-generated magnetic field in the plasma. Sodha *et al.* [60] reported the excitation of UH waves by a Gaussian EM beam, taking into account the nonlinear ponderomotive force. A theoretical study on the wave-breaking phenomenon of relativistic UH oscillations in a cold magnetoplasma was reported by Maity *et al.* [61]. They also studied the breaking of linear and nonlinear electrostatic UH oscillation due to the phase mixing in the presence of an inhomogeneous external magnetic field [62]. Computer simulations of upper hybrid and electron cyclotron resonance heating using a relativistic electromagnetic particle code were reported by Lin *et al.* [46]. Their study showed that the energy of an obliquely incident X-wave with a large angle of incidence converts into electrostatic Bernstein waves at the upper-hybrid resonance layer. In all the previous studies, detailed analysis and characterization of energy conversion processes from an X-wave propagating in an inhomogeneous external magnetic field were not explored thoroughly.

In the present study, we have studied the propagation characteristics of an X-wave in a space varying external magnetic field (B_0) using particle-in-cell (PIC) simulations. In our simulations, the laser was considered to be incident normal to the plasma surface, and intensity was chosen such that relativistic effects can be neglected. It has been shown that as the laser enters inside the plasma, it follows the X-wave dispersion relation. The energy conversion processes from the X-wave to an electrostatic oscillation and eventually to the electron kinetic energy in the vicinity of the UH resonance layer ($\omega_l = \omega_{\rm uh}$) have been investigated. In our study, we have also observed that at the resonance layer, electrostatic upper-hybrid oscillations break and convert their energy to particle kinetic energy. Additionally, we have also observed that some parts of the X-wave energy at the resonant layer convert to a low-frequency lower-hybrid mode and to high-frequency harmonic radiations, which scatter away from the resonance layer. Our study also reveals that the net energy conversion to electrons suffers a loss by increasing the gradient of the external magnetic field. This paper provides a comprehensive analysis of the outcome of upper hybrid oscillations in the presence of an inhomogeneous magnetic field.

This paper is organized as follows: In Sec. II, we have described the simulation set-up and provided the simulation parameters used in our study. Section III contains the observations obtained from the simulation. We have discussed different mode conversion processes from the incident laser beam in the various subsections. Finally, in Sec. IV, we provide a summary of our work.

II. SIMULATION DETAILS

In this study, one-dimensional (1D) PIC simulations have been carried out to study laser's interaction with plasma in the presence of an inhomogeneous external magnetic field. A fully relativistic, massively parallel PIC code, OSIRIS 4.0 [63–65], has been used for this purpose. The 1D simulation geometry considered here has a longitudinal extent of $2500d_e$. Here, d_e represents the electron skin depth $c/\omega_{\rm pe}$, where c is the speed of light in vacuum and $\omega_{\rm pe}$ defines the electron-plasma frequency corresponding to the equilibrium electron density n_0. Plasma boundary starts from $x = 100d_e$. The absorbing boundary conditions have been considered in both the directions for both fields and particles. The number of grid points for our simulation is 50 000, which corresponds to the grid size $dx = 0.05d_e$. The number of particles in each cell is considered to be 8. We choose to normalize the time and length scales by $t_N = \omega_{\rm pe}^{-1}$ and $x_N = c/\omega_{\rm pe} = d_e$, respectively. The fields are normalized by $B_N = E_N = mc\,\omega_{\rm pe}/e$, where m and e represent the mass and the magnitude of the charge of an electron, respectively. The external magnetic field is considered to be along the $\hat{z}$ direction, and the plasma is along the $\hat{x}$ direction, as shown in the schematic Fig. 1(a).

In our simulation, we have considered a laser pulse with a propagation vector $\vec{k}$ along $\hat{x}$, incident on the vacuum-plasma interface from the left side of the plasma. The electric field of the laser ($\vec{E}_l$) is considered to be in the X-mode configuration, i.e., oscillating along $\pm\hat{y}$, as shown in Fig. 1(a). The longitudinal profile of the incident laser pulse is considered to be a polynomial function with a rise and fall time of $30\omega_{\rm pe}^{-1}$, and it starts from $x = 80d_e$. The intensity of the incident laser pulse is considered to be approximately 3.04×10^{13} W/cm^2, corresponding to the normalized vector potential $a_0 = eE_l/m\omega_l c = 0.05$. Here ω_l represents the laser frequency. We have considered the dynamics of both electrons and ions in our study. The mass of the ions is considered to be approximately the same as the proton mass, i.e., $M = 1840m$. In our simulations, the initial temperature of the background plasma is considered to be very low ($T_e = 0.05$ eV). All the plasma and laser parameters that have been used in our simulations are provided in Table I in normalized as well as standard units. The external magnetic

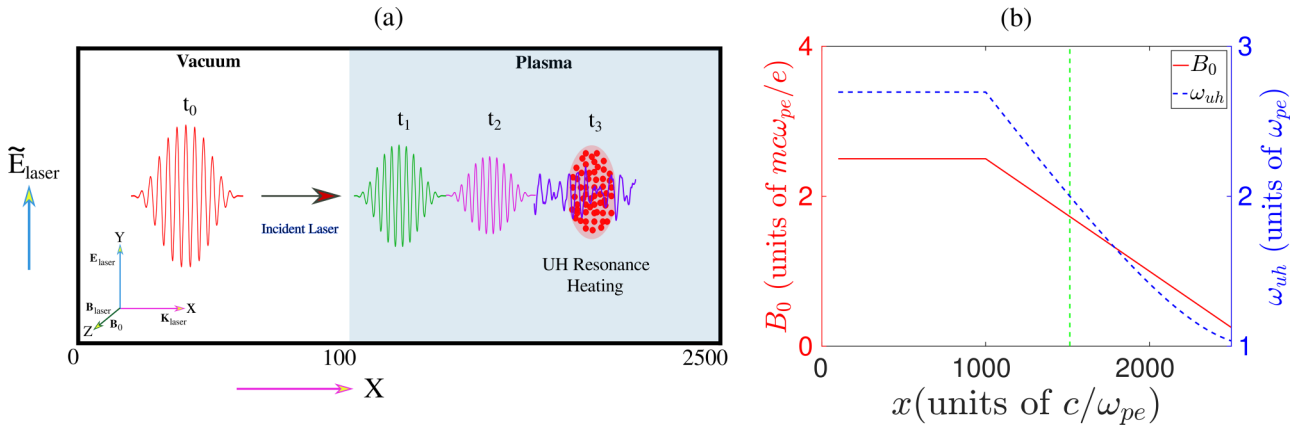

FIG. 1. (a) The simulation setup and a summary of the physical processes observed in our study have been illustrated by this schematic. We have performed 1D PIC simulation with a laser pulse being incident from the left side of the simulation box on the vacuum-plasma interface at $x = 100$. The polarization of the incident laser was considered to be in the X-mode configuration, i.e., $\vec{E}_l \perp \vec{B}_0$. Here t_0, t_1, t_2, and t_3 represent different times (in ascending order) of the simulation run. (b) The external magnetic field and corresponding upper hybrid frequency $\omega_{\rm uh} = \sqrt{\omega_{\rm pe}^2 + \omega_{\rm ce}^2}$ have been shown as a function of x. Here $\omega_{\rm pe}$ and $\omega_{\rm ce}$ represent electron plasma frequency and electron cyclotron frequency, respectively. The green dotted vertical line in panel (b) represents the location at which upper-hybrid resonance ($\omega_l = \omega_{\rm uh}$) occurs.

field B_0 is considered such that it has a constant value equal to $B_0 = 2.5$ (in normalized unit) up to $x = 1000d_e$ and decreases linearly for $x > 1000d_e$, as shown in Fig. 1(b).

III. RESULTS AND DISCUSSION

It is well known that in a magnetized plasma, there are two types of waves that can propagate perpendicular to the external magnetic field ($\mathbf{B}_0$). One is the "ordinary" wave or O-wave where the electric field oscillates parallel to $\mathbf{B}_0$, and the other one is the "extraordinary" wave or X-wave where the electric field of the EM wave oscillates perpendicular to $\mathbf{B}_0$. The dispersion relation of high-frequency X-wave, where the ion motions can be neglected because of their large inertia, is given by [66]

$$\frac{c^2k^2}{\omega^2} = 1 - \frac{\omega_{\rm pe}^2\left(\omega^2 - \omega_{\rm pe}^2\right)}{\omega^2(\omega^2 - \omega_{\rm uh}^2)}. \tag{1}$$

Here $\omega_{\rm pe}$ and $\omega_{\rm uh}$ represent electron plasma frequency and upper-hybrid frequency, respectively. It can be easily shown from Eq. (1) that high-frequency X-wave has two distinct cutoff frequencies (defined when $k \to 0$) as given by

$$\omega_{R,L} = \tfrac{1}{2}\left[\pm\omega_{\rm ce} + \left(\omega_{\rm ce}^2 + 4\omega_{\rm pe}^2\right)^{1/2}\right] \quad . \tag{2}$$

Here the $+$ and $-$ signs stand for the "right-hand" and "left-hand" cutoff frequency, respectively, and $\omega_{\rm ce} = |eB_0/m|$ represents the electron gyration frequency. The dispersion relation given in Eq. (1) also shows that the high-frequency X-wave has a resonance ($k \to \infty$) at the frequency $\omega = \omega_{\rm uh} = \sqrt{\omega_{\rm pe}^2 + \omega_{\rm ce}^2}$, known as the upper-hybrid resonance. The cutoffs and resonance define the pass and stop-bands for the propagation of EM wave inside the plasma. For a high-frequency (ω) X-wave, where the ion motion can be neglected, there exist two pass-bands [(i) $\omega_{\rm uh} \gtrless \omega > \omega_L$, (ii) $\omega > \omega_R$] and one stop-band [$\omega_R > \omega > \omega_{\rm uh}$].

In our PIC study, a laser pulse with a fixed value of frequency ω_l satisfying the condition $\omega_{\rm uh} > \omega > \omega_L$ (i.e., lies in the pass-band) is sent into the plasma from the vacuum. The profiles of the external magnetic field and corresponding upper-hybrid frequency with the position x have been shown in Fig. 1(b). When the laser with frequency $\omega_l = 2.0\omega_{\rm pe}$ is incident on the magnetized plasma surface, it enters inside the bulk plasma as an X-wave and propagates through the

TABLE I. Simulation parameters: In normalized units and possible values in standard units.

Parameters	Normalized value	A possible value in standard unit
	Laser parameters	
Frequency (ω_l)	$2.0\omega_{\rm pe}$	1.78×10^{14} rad/s
Wavelength	$3.14c/\omega_{\rm pe}$	10.6 μm
Intensity	$a_0 = 0.05$	3.04×10^{13} W/cm^2
	Plasma parameters	
Number density (n_0)	1	2.48×10^{18} cm^{-3}
Electron plasma frequency ($\omega_{\rm pe}$)	1	8.86×10^{13} rad/s
Electron skin depth ($c/\omega_{\rm pe}$)	1	3.37 μm
	External fields	
Magnetic field (B_0)	2.5	$\approx$ 6.3 kT

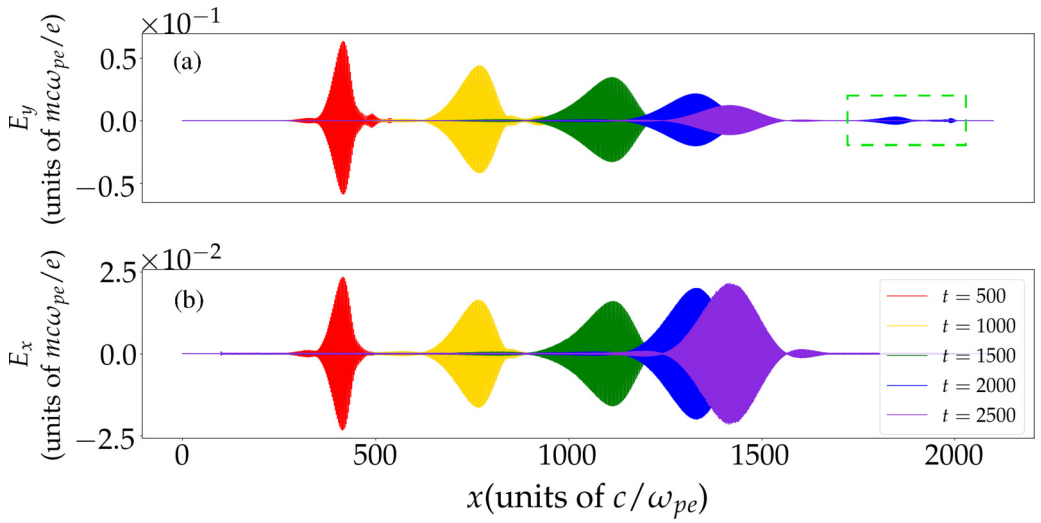

FIG. 2. The $\hat{y}$ and $\hat{x}$ components of electric field $\widetilde{E}_y$ and $\widetilde{E}_x$ with respect to x have been shown at different times of the simulation runs in panels (a) and (b), respectively. Here the x locations of the fields at different times of the simulation run ($t = 500$ to 2500) have been shown by the different colors. The structure highlighted by the green dotted box represent higher harmonics.

plasma until it reaches the UH resonance point shown by the green dotted line in Fig. 1(b). At the UH resonance location, the electromagnetic energy of the X-wave is converted to electrostatic energy and essentially to electron kinetic energy. A summary of the observations of our study has been shown in the schematic in Fig. 1(a). We now present a detailed discussion of various features observed in our simulations in the following subsections.

A. Propagation of X-wave in an inhomogeneous magnetic field

The X-wave propagating perpendicular to $\vec{B}_0$ is partly electromagnetic and partly electrostatic. Thus, it has both transverse and longitudinal components of the electric field. At the upper-hybrid resonance point ($\omega_l = \omega_{\rm uh}$), the transverse component becomes negligible compared to the longitudinal component of the electric field. For an X-wave, the electric field rotates in the clockwise direction, which is opposite to the electron rotation in the external magnetic field. Thus, electron-cyclotron resonance absorption will not occur in the X-mode configuration for a cold, collisionless plasma. However, ECR absorptions may occur even for a perpendicular propagation when collisions, thermal, and relativistic effects become important [39,67]. As the wave propagates through the plasma perpendicular to the inhomogeneous magnetic field B_0, the wave's frequency approaches the upper-hybrid frequency of the medium. Amplitudes of both E_y and E_x decrease initially due to the dispersion of the X-wave as it propagates through the plasma medium. However, as the X-wave enters the inhomogeneous regime ($x > 1000d_e$) of external magnetic field, the amplitude of E_x increases, whereas E_y decreases. This has been shown in Figs. 2(a) and 2(b). The spatial distributions of the electromagnetic (E_y) and electrostatic (E_x) fields at different instants of time from $\omega_{\rm pe}t = 500$ to 2500 have been shown by different colored lines in Figs. 2(a) and 2(b), respectively. It is seen that as the X-wave propagates through the plasma, the amplitude of E_y decreases while the strength of the E_x increases. It can be seen that there is a small segment of E_y which has traveled even beyond the UH resonance layer. This has been highlighted by the green dotted box in Fig. 2(a). Fourier analysis, shown in Fig. 4 reveals that this structure is higher harmonic EM radiation generated from the interaction of incident laser pulse at the vacuum-plasma interface. Since the frequency of this harmonic radiation is higher than the "right-hand" cut-off frequency ω_R, it passes through the UH resonance layer. The consequences of harmonic generation in the present context will also be discussed in Sec. III B.

From the dispersion relation given in Eq. (1) it can be shown [66] that the phase velocity v_p and the group velocity v_g of a high-frequency X-wave for $\omega \to \omega_{\rm uh}$ can be approximately expressed as

$$v_p = \frac{\omega}{k} \approx \frac{c\omega_{\rm uh}(\omega_{\rm uh}^2 - \omega^2)^{1/2}}{\omega_{\rm ce}\omega_{\rm pe}}. \tag{3}$$

$$v_g = \frac{d\omega}{dk} \approx \frac{(\omega_{\rm uh}^2 - \omega^2)^{3/2}c}{\omega_{\rm pe}\omega_{\rm ce}\omega_{\rm uh}}. \tag{4}$$

It is seen from Eqs. (3) and (4) that both the phase and group velocities of the X-wave decrease as we decrease the value of $\omega_{\rm ce}$, i.e., with the decrease of external magnetic field B_0 and become zero for $\omega = \omega_{\rm uh}$. This has been demonstrated in Fig. 3 and also can be observed from Fig. 2. In Fig. 3, the distributions of electromagnetic field (EMF) energy, electrostatic energy $E_x^2/2$ associated with the longitudinal component of electric field E_x, and kinetic energy of electrons in space-time plane have been shown in Figs. 3(a)–3(c), respectively. It is seen that the profiles of energy start curving in the space-time plane at $x > 1000d_e$ and become parallel to the time axis, accompanying a minimal spreading in x at $x \approx 1505d_e$. This can be understood by the fact that the group velocity of the wave decreases as it enters the decreasing regime ($x > 1000d_e$) of the external magnetic field B_0. Finally, at $t \approx 2500$, as the wave-front touches the UH resonance layer ($x \approx 1505d_e$), the wave packet stops

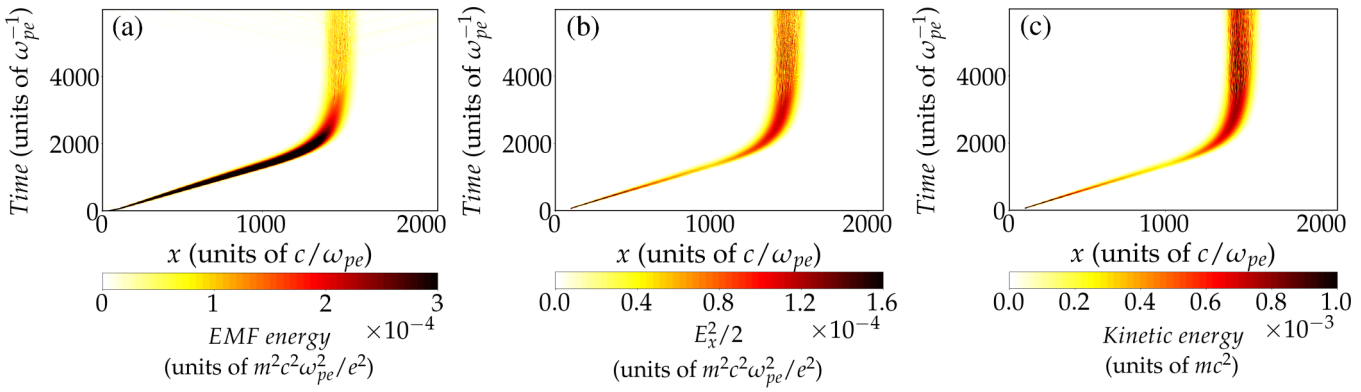

FIG. 3. The variation of (a) electromagnetic field (EMF) energy, (b) energy associated with the longitudinal component of the electric field $E_x^2/2$, and (c) kinetic energy of electron with space and time have been illustrated in panels (a), (b), and (c), respectively.

propagating further, and both its phase and group velocity become zero. At a later time, the energy of this wave packet is converted to electrostatic energy and eventually dissipated to the kinetic energy of plasma particles at the localized region surrounding the UH resonance layer, as shown in Fig. 3. This will also be discussed in further detail in the sections to follow.

The absolute amplitudes of the Fourier spectra obtained from the time-series data of E_y and E_x in different time durations and at various x locations have been shown in Figs. 4(a) and 4(b), respectively. As expected, it is clearly seen that the wave's frequency remains constant (same as the incident laser frequency $\omega_l = 2.0\omega_{\rm pe}$) as it propagates through the medium. It is to be noted that the amplitude of Fourier spectrum of E_y in time evaluated at the location $x = 1500d_e$ and in-between time $t = 2500$-4500 becomes negligible compared to that of

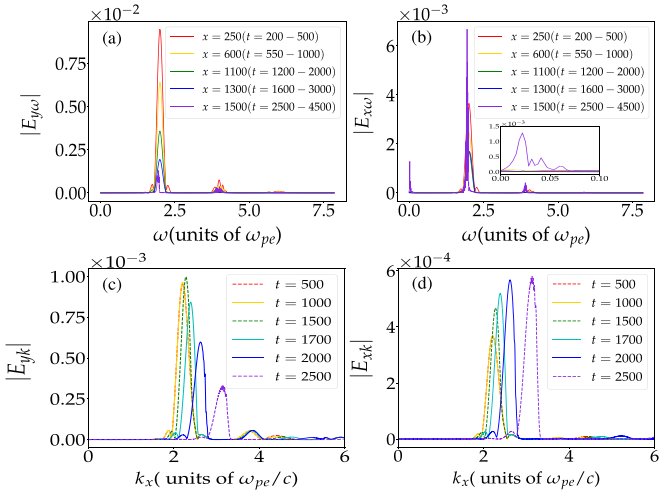

FIG. 4. The absolute amplitudes of Fourier spectra obtained from time-series data of $\widetilde{E}_y$ and $\widetilde{E}_x$ at different x locations have been shown in panels (a) and (b), respectively. It is to be noted that these Fourier spectra have been evaluated at different time durations up to $t = 3500$. The absolute amplitudes of Fourier spectra obtained from the space distributions of $\widetilde{E}_y$ and $\widetilde{E}_x$ at different times of the simulation run have been elucidated by various colored lines in panels (c) and (d), respectively.

E_x. This has been clearly shown by the violet lines in Figs. 4(a) and 4(b), which is a clear indication of the excitation of electrostatic UH oscillation with a frequency $\omega_{\rm uh} = 2.0\omega_{\rm pe}$. In Fig. 4(b), it is also seen that a distinct peak at very low frequency ($\omega \approx 0.02\omega_{\rm pe}$) appears in the Fourier spectrum of E_x evaluated in between $t = 2500$ and 4500 and at the location $x = 1500d_e$. This was not present in the Fourier spectra of E_x evaluated at earlier times, as shown in the inset of Fig. 4(b) and also never appeared in the time Fourier spectrum of E_y. The consequence of this will be discussed in the section to follow. Moreover, in each case, there are also peaks at $\omega = 4\omega_{\rm pe}$ and $6\omega_{\rm pe}$ in the Fourier spectra, representing the higher harmonic radiations. The absolute amplitudes of Fourier spectra obtained from the distributions of E_y and E_x in space at different fixed values of time up to $t = 2500$ have been shown in Figs. 4(c) and 4(d), respectively. It is seen that the Fourier spectra of both E_y and E_x show distinct peaks at a fixed value of $k_x \approx 2.23$ up to $t = 1000$. This is because the X-wave remains within the homogeneous regime of external magnetic field up to $t = 1000$, as can be seen from Fig. 2. It is to be noted that the wave's phase velocity (ω/k) is less than the value of c. This is expected as the frequency of the X-wave is higher than the value of $\omega_{\rm pe}$. Now, as we look at the space Fourier spectra at later times, it is seen that the value of k_x at which the Fourier spectra show distinct peaks is shifted to the higher values. This is the consequence of the fact that the phase velocity decreases as the X-wave enters the decreasing regime of the external magnetic field. In the Fig. 4, it is also seen that the peak value of Fourier spectra of E_y decreases while it increases for E_x. This is consistent with the results shown in Fig. 2.

B. Electron heating and mode conversion at UH resonance layer

In this section, we will discuss the later stage of evolution of the X-wave in the vicinity of the UH resonance layer. To have a close look at the evolution of field profiles at the UH resonance layer, we have shown in Fig. 5 the space distributions of E_y and E_x surrounding the UH resonance layer at different fixed times from $t = 2500$ to 4000. Amplitude of the transverse component of electric field E_y increases up to $t = 3000$. This is because as soon as the front of the wave touches the resonance layer, its group velocity goes to

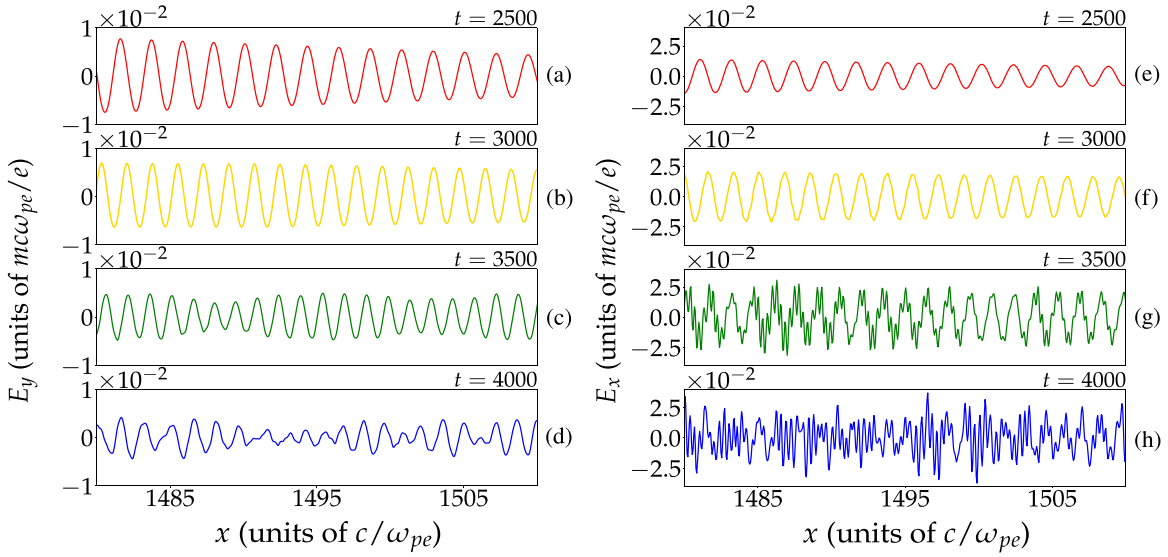

FIG. 5. The zoomed view of $\hat{y}$ and $\hat{x}$ components of electric field E_y and E_x have been shown as function of x for different instants of time in the later phase of the simulation run.

zero, and wave energy density continues to build up in the vicinity of the resonance layer. It is also to be noted that up to $t = 3000$, amplitude of the electrostatic component of electric field E_x also increases and both E_x and E_y have a nice sinusoidal form, as seen in Figs. 5(a) and 5(b) and Figs. 5(e) and 5(f). As time goes on, the sinusoidal form of E_y starts to deform, and wave packets appear in the profile of E_y, as shown in Figs. 5(c) and 5(d). At the same time, the amplitude of E_x further increases, and its sinusoidal form starts to break, as shown in Figs. 5(g) and 5(h).

We have also analyzed the time history of electron and ion density profile in space and shown in Fig. 6. The electron density increases in vicinity of UH resonance layer, whereas ions remain unperturbed (except noisy fluctuations) up to $t = 3000$, as shown in Figs. 6(a) and 6(b) and Figs. 6(e) and 6(f). It is also to be noted that until this time, the electron density profile remains sinusoidal, which is consistent with the E_x profile shown in Figs. 5(e) and 5(f). As time evolves, the electron density further increases. Instead of having a sinusoidal profile, large-amplitude spikes appear in the density profiles, as shown in Figs. 6(c) and 6(d). At the same time, disturbances in the ion density start to appear, and as time goes on, ion density fluctuations increase along with the appearance of density spikes. This has been shown in Figs. 6(g) and 6(h). The frequency of the UH wave is too high to lead any significant modulation of the ion density. The ion density is perturbed due to the excitation of lower-hybrid mode via parametric decay instability near the UH resonance layer. This is also apparent from the Fourier spectra of E_x in time shown in Fig. 4(b). It is seen that a distinct peak at the location $\omega \approx 0.02\omega_{\rm pe}$ appears only at the

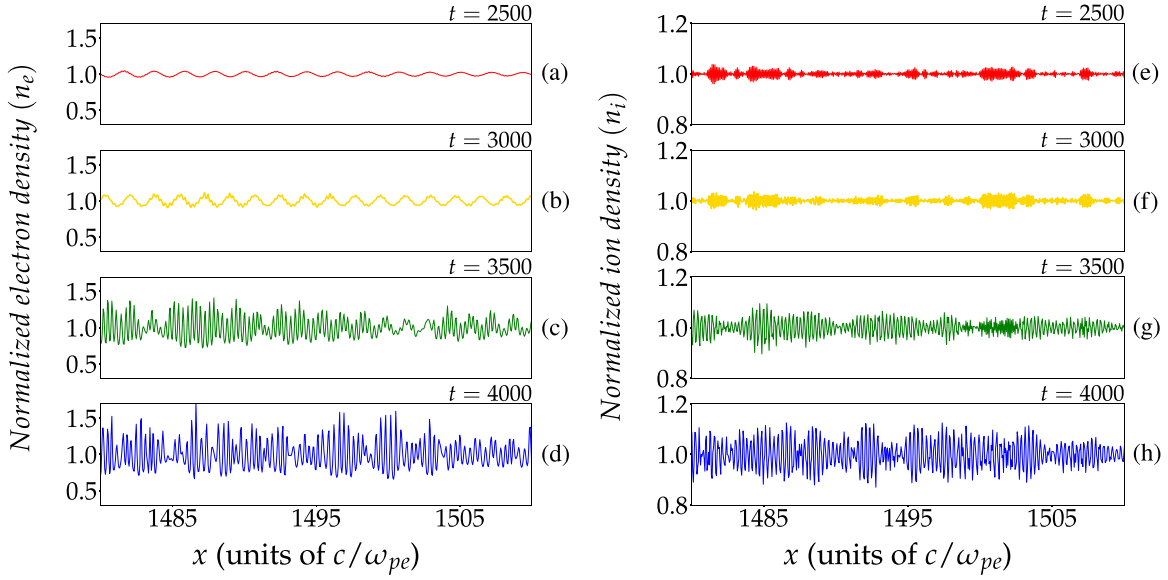

FIG. 6. In (a)–(d), the variation of electron density with x have been shown at different instants of time. Panels (e)–(h) illustrate the same for ion density.

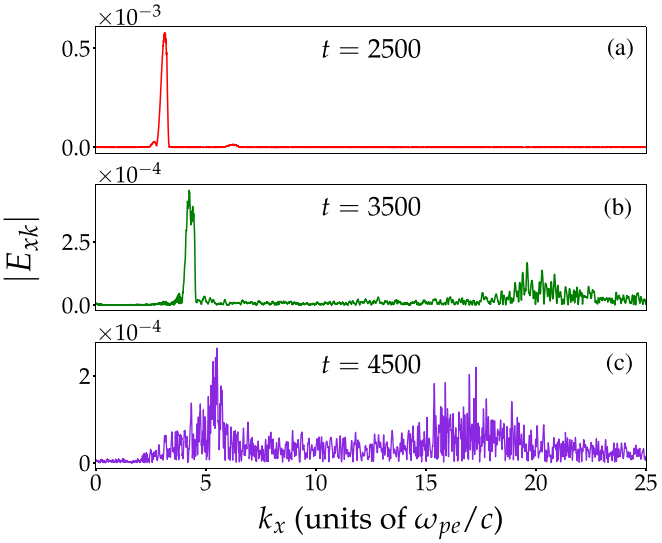

FIG. 7. The absolute amplitudes of Fourier spectra obtained from the space distribution of longitudinal electric field E_x at (a) $t = 2500$, (b) $t = 3500$, and (c) $t = 4500$ have been shown.

later time ($t = 2500$-4500) in the Fourier spectra of E_x, which is approximately same as the lower-hybrid frequency given by [68]

$$\omega_{\rm lh} = \sqrt{\omega_{\rm ce}\omega_{\rm ci}\left(\frac{\omega_{\rm pe}^2 + \omega_{\rm ce}\omega_{\rm ci}}{\omega_{\rm uh}^2}\right)}. \tag{5}$$

Thus, the delay in ion density fluctuations is related to the time it takes a parametric decay instability near UH resonance to excite a significant number of lower-hybrid waves that can eventually perturb the ions. This result demonstrates mode conversion of the high-frequency upper-hybrid oscillation into a low-frequency lower-hybrid mode. It would be interesting to see in future the wave-number-frequency spectra [52] of the longitudianl electric field E_x to identify these wave-wave interaction processes in more detail. The appearance of the spikes in the electron and ion density profiles confirms the breaking of electrostatic mode, which was also indicated in Figs. 5(g) and 5(h). The breaking of UH oscillation in an inhomogeneous external magnetic field was reported in Ref. [62]. In their study, the electrostatic UH oscillation breaks due to phase mixing in the presence of an inhomogeneous external magnetic field. However, in our study, it is unclear whether the nonlinearity, inhomogeneity in B_0, or both, are responsible for breaking electrostatic UH waves.

To further characterize the UH wave-breaking phenomena observed in our simulations, we have also done the Fourier analysis of the electrostatic component E_x in space in the later stage of the evolution. The absolute amplitudes of Fourier spectra evaluated from the space profiles of E_x at fixed times $t = 2500$, 3500, and 4500 have been shown in Figs. 7(a)–7(c), respectively. It is seen that only a sharp, distinct peak appears in the Fourier spectra of E_x at $t = 2500$, and the particular value of k_x where this peak is located can be exactly obtained from the theoretical dispersion relation of the X-wave. As time goes on, fluctuations at higher k_x values also starts to appear in the Fourier spectra of E_x, as shown in Fig. 7(b). This is because after $t \approx 3500$, the electrostatic oscillation starts to break, as illustrated in Fig. 5 and 6 and thus, energy flows to the higher modes. As time increases further, it is seen from Fig. 7(c) that the power of the modes with higher values of k_x increases. This is an indication of wave-particle interaction where energy flows from large to smaller scales.

To illustrate electron heating more distinctly, we have shown the electron energy distributions at three different instants of time of the simulation run in Fig. 8(a). It is seen that as time evolves, the distribution function generates high-energy tails indicating particle heating. In Fig. 8(b), we have shown the time evolution of space-averaged electron kinetic energy (red), ion kinetic energy (yellow), energy associated with the electrostatic field, $E_x^2/2$ (blue), and energy associated with the transverse components of the EM fields, $E_y^2/2 + B_z^2/2$ (green dotted line). This figure clearly illustrates a complete picture of the energy-conversion processes throughout the simulation run. As soon as the laser hits the plasma surface, electron kinetic energy increases. At the same time, electrostatic field energy ($E_x^2/2$), which was not present before, is also produced at the cost of electromagnetic energy ($E_y^2/2 + B_z^2/2$) of the incident laser pulse. Then, as long as the laser (X-wave) propagates inside the plasma within the homogeneous external magnetic field regime, electron kinetic energy, electrostatic energy, and electromagnetic energy remain constant. As the X-wave enters in the decreasing region of B_0 at $t \approx 1300$, the electrostatic energy and electron kinetic energy start to increase, whereas electromagnetic energy decreases. At the time $t \approx 2900$, when the X-wave has already reached the UH resonance layer, the electrostatic energy reaches a maximum value, whereas electron kinetic energy keeps increasing. Finally, at $t \approx 4000$, electron kinetic energy reaches a maximum value, and at the same time, the electromagnetic energy becomes almost zero. It is to be noted that at this time, the electrostatic energy is in a decreasing trend from its peak value, as some parts of its energy are being converted to electron kinetic energy through wave breaking. However, it is interesting to notice that as time further increases, in between $t \approx 4000$-6000, the electromagnetic energy increases again from its minimum value. At the same time, both electrostatic and electron kinetic energy continues to drop until they get saturated. It indicates that there must be a reverse-conversion process where electrostatic energy gets converted to electromagnetic field energy. It is also to be noted that after $t = 4000$, ions have started to gain kinetic energy. This has also been depicted clearly in Fig. 11(a).

In order to have a deeper understanding of the mechanism involved in the mode conversion between electrostatic and electromagnetic field energies, we have observed the spatial distribution of E_y at different instants of time after the X-wave reaches the UH resonance layer and shown in Fig. 9(a). It is interesting to see that at a later time ($t = 4500$), a part of E_y is scattered in the form of wave packets on both sides of the resonance layer. It is to be noted that the original X-wave was neither supposed to cross the resonance layer nor reflect from the resonance layer. In order to further analyze this scattered electromagnetic radiation, we have evaluated the Fourier spectra of E_y in time at two different locations ($x = 1000d_e$ and $1800d_e$) on both sides of the resonance layer and shown in Figs. 9(b1) and 9(b2). The Fourier spectra show

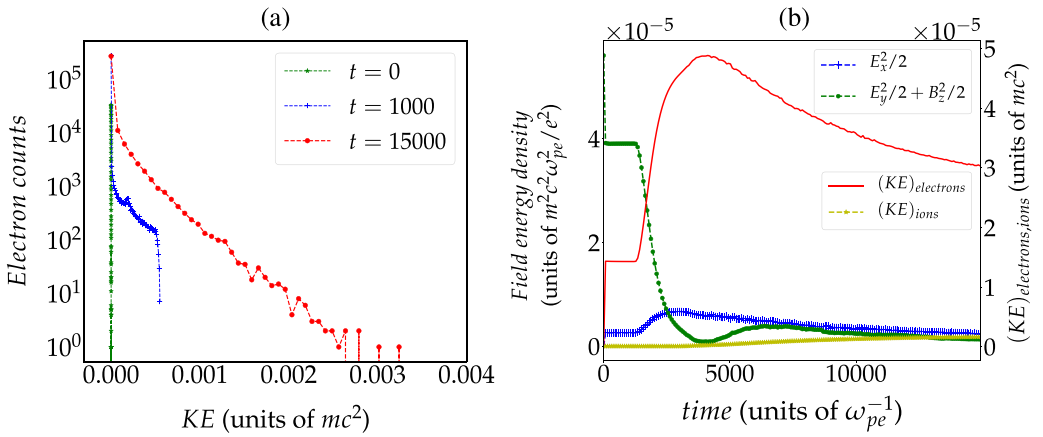

FIG. 8. (a) Electron counts as a function of kinetic energy at three different instants of time of the simulation run have been shown. (b) The time variation of spatially averaged field energy densities have been shown. Here red, yellow, blue, and green colored lines represent kinetic energies of electrons and ions, energy density associated with the longitudinal electric field, and energy density associated with the transverse components of electromagnetic fields, respectively.

that higher harmonics mainly dominate in these scattered radiations with frequencies $4.0\omega_{\rm pe}$ and $6.0\omega_{\rm pe}$. The higher harmonic generation in the presence of an external magnetic field in X and O-mode configurations were shown in detail in our previous study [35]. In the present study also, the basic mechanism of harmonic generation is similar as reported in Ref. [35]. Near the UH resonance layer, where the group velocity of the X-wave becomes approximately zero, nonlinear electron dynamics under the Lorentz force associated with the fields of X-wave and the external static magnetic field B_0 form oscillating currents. These oscillating currents near the UH resonance layer behave like a current antenna and radiate electromagnetic waves with higher frequencies (higher harmonics) along $\pm\hat{x}$ directions, i.e., on both sides of the resonance layer. Let us now try to understand briefly what happened at the UH resonance layer. As the X-wave reaches the resonance layer, its electromagnetic energy eventually converts to electrostatic energy. A part of the X-wave energy also converts to the lower-hybrid modes via parametric instability in the vicinity of the UH resonance layer resulting in an increase of ion kinetic energy. The field energy of the upper-hybrid electrostatic mode is then converted via wave breaking to the electron kinetic energy resulting in heating. At the same time, a part of the electrostatic field (E_x) which is oscillating with the upper-hybrid frequency ($2.0\omega_{\rm pe}$), gets converted to the high harmonic radiation in the presence of an external magnetic field and scattered away in both sides of the resonance layer, which finally gets absorbed at the boundaries. Thus, in this process, some parts of electrostatic energy are also converted to electromagnetic energy, as seen in Fig. 8.

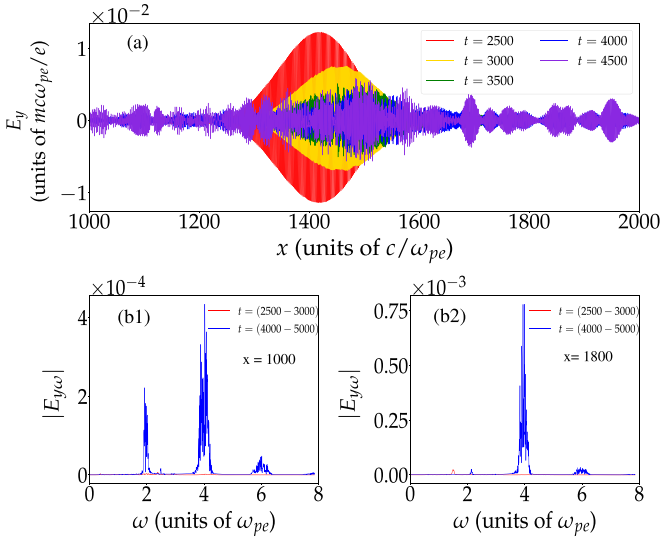

FIG. 9. The space variation of $\hat{y}$ component of electric field has been shown at different times in the later stage of the simulation run in panel (a). The absolute amplitudes of Fourier spectra obtained from the time-series data of E_y at the locations $x = 1000$ and $x = 1800$ for time durations $t = (2500\text{-}3000)$ (red), and $t = (4000\text{-}5000)$ (blue) have been shown in panels (b1) and (b2), respectively.

C. Effect of external magnetic field profile

We have also studied the effect of the external magnetic field (B_0) profile on the energy conversion processes. For this purpose, we have considered four different B_0 profiles shown in Fig. 10(a). It is to be noted that in all four cases, B_0 is kept constant with a value 2.5 (in normalized unit) up to $x = 1000d_e$. We have shown the time evolution of electron kinetic energy in Fig. 10(b) for all these four cases. It is seen that electron kinetic energy attains the maximum value earliest for the B_0 profile with the highest gradient. This is because for the steeper B_0 profiles, the resonance layer is located at the smaller values of x, and thus, X-wave takes a shorter time to reach the resonance layer. It is also interesting to notice that the rate of decrease of the electron kinetic energy from its peak value is higher for the case with the B_0 profile having a steeper slope. This has been clearly illustrated in Fig. 10(c). Thus, the net energy converted irreversibly to the electrons, resulting an increase in electron kinetic energy, will be high for the case with a B_0 profile having a gentle slope.

Let us now try to understand why the energy conversion process has such a dependency on the external magnetic field profile. As discussed in the previous section, the two physical

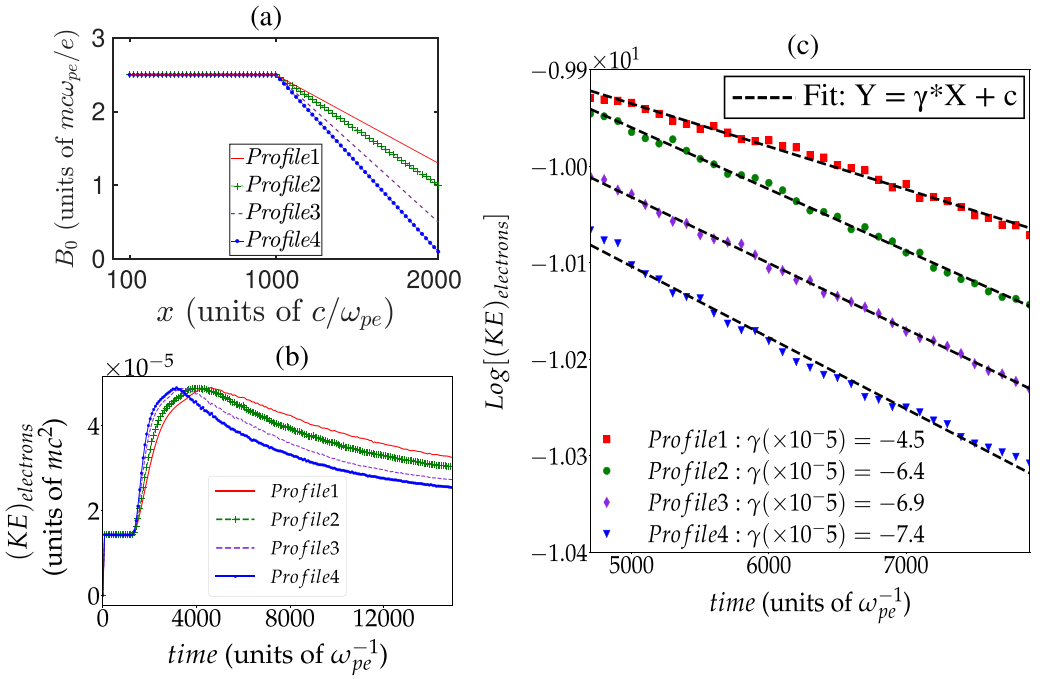

FIG. 10. (a) The four different external magnetic field profiles considered in our simulations have been shown. (b) The variation of electron kinetic energy with time has been demonstrated for these four different external magnetic field (B_0) profiles. (c) The decaying parts of the electron kinetic energy for each case have been shown along with the linearly fitted lines.

processes are mainly responsible for the decay of electrostatic mode and electron kinetic energy. One is the energy conversion to the ions through the lower-hybrid modes excited via parametric decay instability at the UH resonance layer. The other is the energy conversion to the higher electromagnetic harmonics, which eventually radiate out from the resonance layer and get absorbed at the boundaries. In our study, we have observed that the efficiency of both these energy conversion mechanisms involved in the decay of electron kinetic energy increases with the steeper B_0 profiles. This has been illustrated in Fig. 11. It can be seen from Fig. 11(a) that the rate of increase of ion kinetic energy is higher for steeper B_0 profiles. Thus, the net energy converted to ions via lower-hybrid mode excitation increases with the steepness of B_0. The increase of harmonic generation efficiency with the steeper B_0 profiles has been demonstrated in Figs. 11(b) and 11(c). It can be seen from Fig. 11(b) that the transverse EMF energy at first increases with time in between time $\omega_{pe}t = 4000$-6000. It can also be seen from Fig. 11(b) and the inset that the rate of increase of transverse EMF energy during this period is higher for steeper B_0 profiles. In the previous section (Fig. 9), we have discussed that generation of higher harmonic is responsible for this increase of EMF energy in the later phase of the evolution. Thus, we can say that the efficiency of harmonic generation increases with the increase of gradient of B_0 profiles. Consequently, for the steeper magnetic field profiles, more electromagnetic energy radiates out from the resonance layer in the form of harmonics and gets absorbed at the bound-

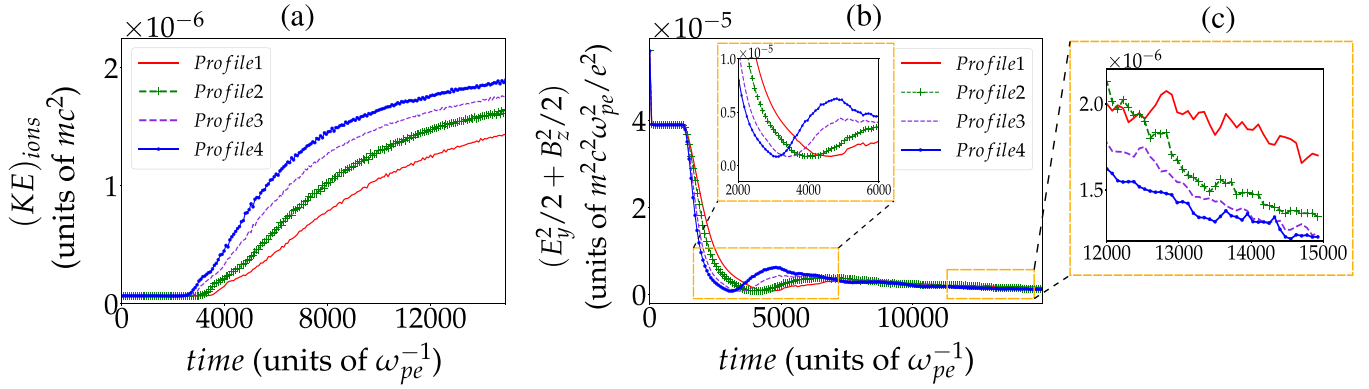

FIG. 11. The variation of ion kinetic energy with time has been shown in panel (a) for four different externally applied magnetic field (B_0) profiles. In the panel (b), we have shown the time evolution of spatially averaged energy densities associated with the transverse components of electromagnetic fields, i.e., $E_y^2/2 + B_z^2/2$ for these profiles of B_0. In panel (c) and panel (b) inset, transverse EMF energy has been shown in zoomed scale.

aries. Thus, in the later phase of simulation runs, EM energy remaining inside the plasma is less for the steeper profiles, as can be seen in Fig. 11(c). The increase of harmonic generation efficiency with the gradient of the B_0 profile can be understood as follows. In an earlier study [35], it has been shown that the efficiency of harmonic generation strongly depends on the value of an external magnetic field. The harmonic generation efficiency attains a maximum value for a particular value of B_0 where the condition $\omega_{ce} = 2\omega_l$ is satisfied and it increases with B_0 in the regime $\omega_{ce} < 2\omega_l$. In the present study, at the upper-hybrid resonance layer ($\omega_l = \omega_{uh}$), the condition $\omega_{ce} < 2\omega_l$ is always satisfied. We have shown that as the front of the X-wave touches the resonance layer, it stops propagating further. Since the X-wave has a finite longitudinal extend, it will face different values of B_0 at different x-locations in the vicinity of the resonance layer. However, the mean value of B_0 over the longitudinal length of the wave is higher for a B_0 profile with a steeper gradient. Thus, the harmonic generation efficiency increases for a steeper B_0 profile. As a result, more energy radiates away from the resonance layer via harmonics and is absorbed at the boundaries. Thus, the available energy to convert to electron kinetic energy becomes less.

IV. SUMMARY

The characteristics of the extraordinary wave (X-wave) originated from the interaction of a laser beam with a magnetized plasma are studied using PIC simulations. It has been shown that the group velocity and phase velocity of X-wave changes as it propagates under an inhomogeneous magnetic field and essentially goes to zero as it reaches the upper-hybrid resonance point. The energy conversion from the X-wave to the UH electrostatic mode at the resonance layer has been shown. These electrostatic waves essentially break and convert their energy to electrons in the vicinity of the resonance layer. Additionally, our study also reveals that two additional processes are involved in the decay of electrostatic oscillations at the UH resonance layer. A part of the X-wave energy in the vicinity of the UH resonance layer converts to the lower-hybrid modes causing ion density fluctuations and heating. A significant portion of the energy associated with the UH electrostatic modes also converts to the high-frequency harmonic EM radiation and is scattered away from the resonant location. In our study, we have shown that the net energy absorbed by electrons depends on the profile of the external magnetic field. Our study reveals that electrons gain more kinetic energy for an external magnetic field profile with a gentler slope. On the other hand, the conversion efficiency to harmonic radiation and ion kinetic energy can be increased by increasing the gradient of the external magnetic profile.

ACKNOWLEDGMENTS

The authors thank IIT Delhi HPC facility for computational resources. The authors would like to acknowledge the OSIRIS Consortium, consisting of UCLA (U.S.) and IST (PT) for providing access to the OSIRIS 4.0 framework which is the work supported by the NSF (U.S.), ACI-1339893. This work was supported by the J.C. Bose fellowship grant (A.D., Grant No. JCB/2017/000055/SSC) from the Department of Science and Technology (DST), Government of India and by the Core Research Grant (A.D., Grant No. CRG/2018/000624) of the Science and Engineering Research Board (SERB), Government of India.

[1] P. Kaw, Rev. Mod. Plasma Phys. **1**, 2 (2017).
[2] K. A. Brueckner and S. Jorna, Rev. Mod. Phys. **46**, 325 (1974).
[3] S. Atzeni and J. Meyer-ter Vehn, *The Physics of Inertial Fusion: Beam Plasma Interaction, Hydrodynamics, Hot Dense Matter* Vol. 125 (Oxford University Press, Oxford, 2004).
[4] B. Zohuri, *Inertial Confinement Fusion Driven Thermonuclear Energy* (Springer, Berlin, 2017).
[5] T. Tajima and J. M. Dawson, Phys. Rev. Lett. **43**, 267 (1979).
[6] C. Joshi, W. Mori, T. Katsouleas, J. Dawson, J. Kindel, and D. Forslund, Nature (London) **311**, 525 (1984).
[7] A. Modena, Z. Najmudin, A. Dangor, C. Clayton, K. Marsh, C. Joshi, V. Malka, C. Darrow, C. Danson, D. Neely *et al.*, Nature (Lond.) **377**, 606 (1995).
[8] A. Macchi, M. Borghesi, and M. Passoni, Rev. Mod. Phys. **85**, 751 (2013).
[9] R. K. Bera, S. Sengupta, and A. Das, Phys. Plasmas **22**, 073109 (2015).
[10] R. K. Bera, A. Mukherjee, S. Sengupta, and A. Das, Phys. Plasmas **23**, 083113 (2016).
[11] R. K. Bera, D. Mandal, A. Das, and S. Sengupta, AIP Adv. **10**, 025203 (2020).
[12] A. Rousse, K. T. Phuoc, R. Shah, A. Pukhov, E. Lefebvre, V. Malka, S. Kiselev, F. Burgy, J.-P. Rousseau, D. Umstadter, and D. Hulin, Phys. Rev. Lett. **93**, 135005 (2004).
[13] S. Corde, K. Ta Phuoc, G. Lambert, R. Fitour, V. Malka, A. Rousse, A. Beck, and E. Lefebvre, Rev. Mod. Phys. **85**, 1 (2013).
[14] S. Cipiccia, M. R. Islam, B. Ersfeld, R. P. Shanks, E. Brunetti, G. Vieux, X. Yang, R. C. Issac, S. M. Wiggins, G. H. Welsh *et al.*, Nat. Phys. **7**, 867 (2011).
[15] B. A. Remington, R. P. Drake, H. Takabe, and D. Arnett, Phys. Plasmas **7**, 1641 (2000).
[16] P. K. Kaw, A. Sen, and T. Katsouleas, Phys. Rev. Lett. **68**, 3172 (1992).
[17] D. Verma, R. K. Bera, A. Kumar, B. Patel, and A. Das, Phys. Plasmas **24**, 123111 (2017).
[18] D. Verma, A. Das, P. Kaw, and S. K. Tiwari, Phys. Plasmas **22**, 013101 (2015).
[19] S. Poornakala, A. Das, A. Sen, and P. K. Kaw, Phys. Plasmas **9**, 1820 (2002).
[20] S. Poornakala, A. Das, P. K. Kaw, A. Sen, Z. M. Sheng, Y. Sentoku, K. Mima, and K. Nishikawa, Phys. Plasmas **9**, 3802 (2002).
[21] S. Sundar, A. Das, V. Saxena, P. Kaw, and A. Sen, Phys. Plasmas **18**, 112112 (2011).
[22] D. Mandal, A. Vashistha, and A. Das, J. Plasma Phys. **86**, 905860606 (2020).
[23] J. Stamper, K. Papadopoulos, R. Sudan, S. Dean, E. McLean, and J. Dawson, Phys. Rev. Lett. **26**, 1012 (1971).

[24] S. C. Wilks, W. L. Kruer, M. Tabak, and A. B. Langdon, Phys. Rev. Lett. **69**, 1383 (1992).
[25] P. Gibbon, Phys. Rev. Lett. **73**, 664 (1994).
[26] A. Das, A. Kumar, C. Shukla, R. K. Bera, D. Verma, D. Mandal, A. Vashishta, B. Patel, Y. Hayashi, K. A. Tanaka, G. Chatterjee, A. D. Lad, G. R. Kumar, and P. Kaw, Phys. Rev. Research **2**, 033405 (2020).
[27] K. R. Manes, V. C. Rupert, J. M. Auerbach, P. Lee, and J. E. Swain, Phys. Rev. Lett. **39**, 281 (1977).
[28] J. S. Pearlman, J. J. Thomson, and C. E. Max, Phys. Rev. Lett. **38**, 1397 (1977).
[29] K. Estabrook and W. L. Kruer, Phys. Rev. Lett. **40**, 42 (1978).
[30] F. Brunel, Phys. Rev. Lett. **59**, 52 (1987).
[31] T.-Y. B. Yang, W. L. Kruer, R. M. More, and A. B. Langdon, Phys. Plasmas **2**, 3146 (1995).
[32] E. Lefebvre and G. Bonnaud, Phys. Rev. E **55**, 1011 (1997).
[33] W. Kruer and K. Estabrook, Phys. Fluids **28**, 430 (1985).
[34] A. Vashistha, D. Mandal, A. Kumar, C. Shukla, and A. Das, New J. Phys. **22**, 063023 (2020).
[35] S. Maity, D. Mandal, A. Vashistha, L. P. Goswami, and A. Das, J. Plasma Phys. **87**, 905870509 (2021).
[36] D. Mandal, A. Vashistha, and A. Das, Sci. Rep. **11**, 14885 (2021).
[37] L. P. Goswami, S. Maity, D. Mandal, A. Vashistha, and A. Das, Plasma Phys. Controlled Fusion **63**, 115003 (2021).
[38] R. Geller, *Electron Cyclotron Resonance Ion Sources and ECR Plasmas* (Routledge, London, 2018).
[39] M. Bornatici, R. Cano, O. De Barbieri, and F. Engelmann, Nucl. Fusion **23**, 1153 (1983).
[40] V. Erckmann and U. Gasparino, Plasma Phys. Control. Fusion **36**, 1869 (1994).
[41] H. P. Laqua, V. Erckmann, H. J. Hartfuß, and H. Laqua, Phys. Rev. Lett. **78**, 3467 (1997).
[42] A. Ganguli, R. Tarey, R. Narayanan, and A. Verma, Plasma Sourc. Sci. Technol. **28**, 035014 (2019).
[43] T. H. Stix, Phys. Rev. Lett. **15**, 878 (1965).
[44] A. T. Lin and C.-C. Lin, Phys. Rev. Lett. **47**, 98 (1981).
[45] A. Lin, C.-C. Lin, and J. Dawson, Phys. Fluids **25**, 646 (1982).
[46] A. Lin and C. C. Lin, Phys. Fluids **26**, 3612 (1983).
[47] R. Stenzel and R. Gould, J. Appl. Phys. **42**, 4225 (1971).
[48] B. Grek and M. Porkolab, Phys. Rev. Lett. **30**, 836 (1973).
[49] Y. M. Peng, S. Borowski, and T. Kammash, Nucl. Fusion **18**, 1489 (1978).
[50] A. Köhn, G. Birkenmeier, A. Chusov, P. Diez, A. Feuer, U. Höfel, H. Höhnle, E. Holzhauer, W. Kasparek, S. Merli *et al.*, Plasma Phys. Control. Fusion **55**, 014010 (2013).
[51] A. Arefiev, I. Dodin, A. Köhn, E. D. Toit, E. Holzhauer, V. Shevchenko, and R. Vann, Nucl. Fusion **57**, 116024 (2017).
[52] M. G. Senstius, S. K. Nielsen, R. G. Vann, and S. K. Hansen, Plasma Phys. Control. Fusion **62**, 025010 (2020).
[53] S. K. Hansen, S. K. Nielsen, M. Salewski, M. Stejner, and J. S. and, Plasma Phys. Control. Fusion **59**, 105006 (2017).
[54] C. J. Bryers, M. J. Kosch, A. Senior, M. T. Rietveld, and T. K. Yeoman, J. Geophys. Res.: Space Phys. **118**, 7472 (2013).
[55] M. Lee and S. Kuo, J. Plasma Phys. **30**, 463 (1983).
[56] R. Sharma and P. Shukla, Phys. Fluids **26**, 87 (1983).
[57] D. Nakamura, A. Ikeda, H. Sawabe, Y. Matsuda, and S. Takeyama, Rev. Sci. Instrum. **89**, 095106 (2018).
[58] C. Grebogi, C. S. Liu, and V. K. Tripathi, Phys. Rev. Lett. **39**, 338 (1977).
[59] Y. Kitagawa, Y. Yamada, I. Tsuda, M. Yokoyama, and C. Yamanaka, Phys. Rev. Lett. **43**, 1875 (1979).
[60] M. Sodha, D. Tewari, B. Patheja, and R. Sharma, J. Plasma Phys. **21**, 267 (1979).
[61] C. Maity, A. Sarkar, P. K. Shukla, and N. Chakrabarti, Phys. Rev. Lett. **110**, 215002 (2013).
[62] C. Maity, N. Chakrabarti, and S. Sengupta, Phys. Rev. E **86**, 016408 (2012).
[63] R. G. Hemker, arXiv:1503.00276 (2015).
[64] R. A. Fonseca, L. O. Silva, F. S. Tsung, V. K. Decyk, W. Lu, C. Ren, W. B. Mori, S. Deng, S. Lee, T. Katsouleas *et al.*, *OSIRIS: A Three-Dimensional, Fully Relativistic Particle in Cell Code for Modeling Plasma Based Accelerators* (Springer, Berlin, 2002), pp. 342–351.
[65] R. A. Fonseca, S. F. Martins, L. O. Silva, J. W. Tonge, F. S. Tsung, and W. B. Mori, Plasma Phys. Control. Fusion **50**, 124034 (2008).
[66] R. J. Goldston, *Introduction to Plasma Physics* (CRC Press, Boca Raton, FL, 2020).
[67] S. Hansen, S. Nielsen, J. Stober, J. Rasmussen, M. Salewski, M. Stejner, and A. U. Team, Phys. Plasmas **26**, 062102 (2019).
[68] D. G. Swanson, *Plasma Waves*, Series in Plasma Physics (Institute of Physics, Bristol, UK, 2003).